International Journal of Heat and Fluid Flow 29 (2008) 812–819

Contents lists available at ScienceDirect

International Journal of Heat and Fluid Flow

journal homepage: www.elsevier.com/locate/ijhff

Unsteady wall pressure field of a model A-pillar conical vortex

C. Hoarau, J. Borée *, J. Laumonier, Y. Gervais

Laboratoire d'Etudes Aérodynamiques, LEA UMR CNRS/Université de Poitiers/ENSMA 6609, Téléport 2, 1 Av. Clément Ader, BP 40109, 86961 Futuroscope Chasseneuil, France

ARTICLE INFO

Article history:
Received 19 October 2007
Received in revised form 12 February 2008
Accepted 14 February 2008
Available online 14 April 2008

Keywords:
Turbulent aerodynamics
Conical vortex
A-pillar vortex
Fluctuating pressure

ABSTRACT

The spatio-temporal properties of the unsteady wall pressure field of a model A-pillar conical vortex are studied in this paper by combining 2 component LDV measurements and multi-point pressure measurements using off-set microphones. The model body has sharp edges. Detailed LDV measurements are presented and discussed in the vortex region. The fluctuating velocities are the signature of both an unsteady behaviour of the organised vortical structure interacting with the wall and of finer scale turbulence carried by the unsteady flow. A spectral analysis of the fluctuating pressure under the vortex core is used to analyse the link between the temporal and spatial scales of the unsteady aerodynamics and the wall pressure field. We show that the conical vortex is a guide for the velocity perturbations and that their hydrodynamic pressure footprint is transported at the measured mean axial velocity in a local reference frame aligned with the vortex core. Two distinct peaks of coherence can then be associated with perturbations having (i) a length scale of the order of the full length of the conical structure; (ii) a length scale of the order of the width of the structure. These perturbations may correspond to a global meandering of the structure (low frequency contribution) and to large scale perturbations generated during the rolling-up of the unsteady vortex sheet. Notably, the energy containing higher frequency parts of the PSD are only weakly correlated when distant sensors are considered. The three distinct contributions extracted here have a significant impact as far as Cp' is concerned and should be transmitted in very different ways by the car structure because the frequency and length scale range is very distinct.

1. Introduction

Conical vortices generated over surfaces having a swept angle with the incident wind are found in a particularly large class of practical applications. Leading edge vortices that develop over delta-wings have been extensively studied because they provide a significant amount of lift and because their breakdown is critical to fighter aircraft performance (Delery, 1994). Most studies focus on relatively high angles of attack and slender delta-wings. The conical vortex then develops away from the wall and a core axial velocity larger than the freestream velocity is measured (see e.g. Ol and Gharib, 2003 and references therein). The use of particle image velocimetry (PIV) to educe the near-surface topology (Yavuz et al., 2004) is promising because it allows the identification of regions of unsteadiness along the surface of the fixed or moving wing. Less slender wings having low angles of attack and for flows of lower Reynolds numbers where studied by Ol and Gharib (2003) using stereoscopic PIV. A clear modification of the mean and fluctuating characteristics of leading edge vortices in these conditions was clearly established.

Conical vortices are also important features for civil engineering and transport engineering. They are responsible for extreme suction peaks occurring on the roof of low-rise buildings (see e.g. Kawai and Nishimura, 1996; Banks et al., 2000) and their unsteady behaviour over parallelepiped models of buildings is certainly strongly coupled with the complex 3D aerodynamics of these bluff bodies and its interaction with the ground (upstream horse-shoe vortex system, unsteady 3D wake, etc.).

The study presented in this paper has a strong link with the aerodynamic and aero-acoustic of passenger vehicles. More particularly, we focus here on the study of a model A-pillar conical vortex. Previous studies (see Alam et al., 2003 and references therein) have clearly established that the flow around a passenger car's A-pillar region is a major source of "in-cabin" aerodynamic noise. The main source is due to the resultant fluctuating pressure on the vehicle structure. Of course, by means of large A-pillar radii and avoidance of flow separation, aerodynamic noise can be minimised. Unfortunately, such constraints often conflict with style constraints. There is therefore a need for analysis, even in model situations with sharp edges, in order to develop efficient control strategies which are efficient whatever the geometry. An important particularity of these A-pillar structures is their strong interaction with the lateral wall of the car. This differs from delta-wing

* Corresponding author. Tel.: +33 549498094; fax: +33 549498089.
E-mail address: jacques.boree@lea.ensma.fr (J. Borée).

0142-727X/$ - see front matter © 2008 Elsevier Inc. All rights reserved.
doi:10.1016/j.ijheatfluidflow.2008.02.015

leading edge vortices at high angle of attack. This interaction is particularly clear when analysing mean velocity fields around vehicles. For example, a mirror image can be used to qualitatively understand the mean downstream evolution of these structures of concentrated vorticity that shift to the roof of the car when traveling toward the back of the car (Hucho, 1998; Gillieron, 2000; Depardon et al., 2006).

To the authors' knowledge, only a few publications present an accurate study of the fluctuating velocity fields and/or fluctuating pressure fields in these typical flow structures. The paper of Alam et al. (2003) presents a very interesting parametric study of the mean and fluctuating pressure measurements for a family of idealized road vehicles at different yaw angles. Unfortunately, no measurements of the associated velocity field were provided. The maximum fluctuating pressure coefficient is large for a slanted sharp-edged A-pillar (≈30% at 0° yaw angle) and located under the separated conical vortex. Power spectral densities are also presented and preferential Strouhal numbers are identified. However, these Strouhal numbers are based on an arbitrarily chosen length scale and are therefore difficult to associate with particular physical events. This observation motivates the use of multi-point analysis techniques.

Our objectives in the present work were as follows: (i) to present a model geometry that can be used for physical analysis and further control studies (Lehugeur and Gillieron, 2006); (ii) to provide a measurement of the mean and fluctuating velocity field in the conical vortex region; (iii) to provide multi-point measurements of the surface pressure in order to better understand the spatio-temporal evolution of the fluctuating wall pressure.

We believe that the last point is particularly important for aeroacoustic studies. Indeed, not only the temporal characteristics but also the spatial length scales and when possible the determination of the transport properties from a cross-spectral analysis are essential data if one is to understand a side window vibration or flexure. The experimental set-up and measurements techniques are presented in Section 2. Mean and fluctuating velocity fields in the conical vortex and spatio-temporal properties of the fluctuating pressure at the wall are then discussed. A physical discussion is proposed in Section 4. The link between both sets of measurements, with a local reference frame aligned with the core of the vortex being used for the velocity, is believed to clearly highlight the mean transport of the large scale perturbations in the conical vortex, and the associated length scales.

2. Experimental set-up and measurements techniques

A picture of the body is shown in Fig. 1. The length and width of the base are $L = 400$ mm and $W = 120$ mm. The height of the model is $H = 90$ mm. The two lateral sides are inclined at 10° while the angle of the forward facing ramp is 30°. The junction between the ramp and the roof is rounded in order to prevent flow separation on the top of the body. Indeed, such separation would result in a strong coupling between the two A-pillar vortices. All other angles are sharp in order to control the location of flow separation. The body was carefully aligned with the oncoming flow and only a 0° yaw angle is studied here.

The free stream velocity of this study is fixed and equal to $U_\infty = 30$ m/s. The Reynolds number based on H is then $R_{eH} = 1.8 \times 10^5$ and is lower than usual values for car aerodynamics. In Fig. 1, we see that the turbulence of the boundary layer is tripped at the sharp nose. The oil flow visualisation obtained using a mixture of white spirits and kaolin powder shows that the flow remains attached on the body.

The dimensions of the exit section of the 3/4 open throat anechoic wind tunnels are 450 mm × 450 mm. More details concerning the wind tunnel can be found in Hoarau (2006). The blockage ratio of the body plus supporting strut is 6%. The location of the body was chosen according to SAEJ2071 (1994) recommendations for 3/4 open throat wind tunnels. The nose of the body is located at a distance of 200 mm from the exit section of the wind tunnel. Our motivation was here to minimize interactions with the ground. Therefore, the height of the streamlined supporting strut is 100 mm in order to place the body outside the boundary layer knowing that the displacement thickness of the boundary layer at that location and without any model is $\delta^* = 1.2$ mm, leading to a 99% thickness δ of order 10 mm.

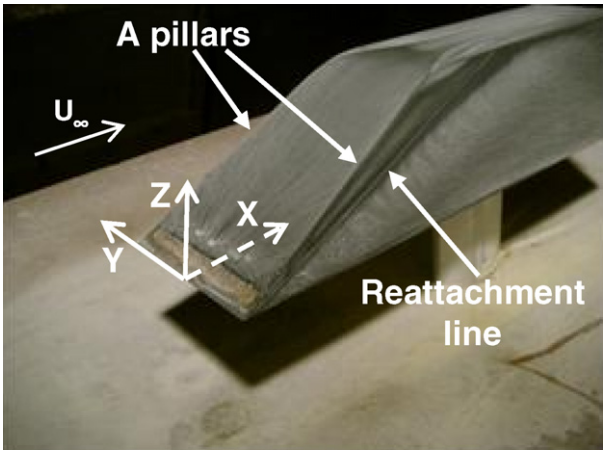

Fig. 1. Picture of the body. Oil flow visualisation obtained by using a mixture of white spirit and kaolin powder.

The velocity measurements are obtained with a two color Laser Doppler Velocimeter (LDV) in backscatter configuration. A global characterisation of the flow around the body is presented in Hoarau (2006). Both longitudinal and vertical velocity components are measured and data obtained in the A-pillar vortex region will be discussed in this paper. The 0.488 μm and 0.5145 μm wavelength beams of an argon-ion laser are used to produce the LDV fringe patterns. The estimated size of the measurement volume is less than 0.1 mm in diameter and 1.3 mm long in the spanwise direction. The mean data rate is always larger than 5 kHz. The inter-arrival time weighting scheme is used to calculate the mean velocities and Reynolds stresses. A regulated glycerine smoke seeding system was specially designed for the wind tunnel and a homogeneous seeding was achieved in the measurement region. The diameter of the smoke particles is of the order of one micrometer. Their time constant is therefore $\tau_p = \rho_p d_p^2/18\mu \approx 3\mu$s, where ρ_p is the density of the particles, d_p their diameter and μ the dynamic viscosity of air. We have checked that they are able to accurately track the turbulent flow in the present experiment.

The flow will be described henceforth using a cartesian co-ordinate system (x, y, z) to indicate the axial, transverse and vertical directions. The origin is set on the symmetry plane and nose of the body (see Fig. 1). The components of the instantaneous velocity field are denoted, respectively by (U, V, W), where U is the longitudinal component and W is the vertical component. Only these components are measured by the present LDV system. The symbol $\langle\ \rangle$ indicates an averaging operator. The components of the instantaneous fluctuating velocity field are denoted respectively by (u, v, w). The expressions u' and w' stand, respectively for longitudinal and vertical standard deviation: $u' = \sqrt{\langle u^2 \rangle}$ and $w' = \sqrt{\langle w^2 \rangle}$. The number of uncorrelated events captured is always larger than 5000. Consequently, estimated statistical absolute errors for mean

values are respectively $\Delta\langle U\rangle \approx 0.03u'$, $\Delta u' \approx 0.02u'$ and $\Delta\langle uw\rangle \approx 0.03u'w'$ with a 95% confidence level.

Measurements of the surface fluctuating pressure are obtained with off-set microphones because the distance between pressure holes can be much smaller than that achieved with flush mounted microphones. The pressure probes comprise electret microphone cartridges which are connected to pressure tabs (inner diameter 0.9 mm) via a pneumatic circuit (a flexible tube of length 0.3 m) (Laumonier et al., 2001). Note that a long tube of 2 m length is connected to each sensor to adapt the impedance and to avoid acoustic resonances. For each probe, the frequency response is measured (magnitude and phase) with a B&K UA 0922 coupler and a reference microphone (see Hoarau et al., 2006 for more details). The signal/noise ratio of the pressure probe is 50 dB. The signal recorder is able to simultaneously acquire 16 pressure probe signals with an effective sampling frequency of 12.8 kHz and a cut-off frequency of the anti-aliasing filters set at 6.4 kHz. The frequency response of each pressure probe is used to correct the magnitude and phase of the spectral functions – Power Spectral Density (PSD), cross-spectrum. The Power Spectral Density (PSD) is estimated with the Welch method. The time series data are split into segments of 2096 points with a 50% overlap. A Hamming window is used to compute the modified periodogram of each segment. The number of segments is 250. Sixteen pressure sensors are located inside the body and all the connecting cables go through the supporting strut. Acquisitions along two lines perpendicular to the inclined edge of the "A-pillar" (lines 1–2 of Fig. 2) will be described in the present paper. The precise location of each pressure tab along each line is provided in Table 1. In Table 1, ξ is the distance from the sharp "A-pillar"; $C_{i,j}$ corresponds to the pressure sensor number j located along line i.

3. Mean and fluctuating velocity field in the conical vortex

Mean and fluctuating velocity fields were measured in a vertical plane located at $x = 100$ mm (100 mm from the nose of the body – see Figs. 2 and 3). Contour plots are presented in Figs. 4 and 5a and b. The mean rotation of the conical vortex is clearly identified in this plane (consider the sign of $\langle W\rangle$ component in the vortex region of Fig. 4b). A mean longitudinal velocity is measured in the vortex core. The vertical dashed line plotted in Figs. 4 and 5 is the vertical line corresponding to the maximum negative value of $\langle W\rangle$ (see Fig. 7). This defines an approximate mean edge of the vortex. We learn from Figs. 5a and b that high values of $\langle uu\rangle$ and $\langle ww\rangle$ are detected inside the structure only. To be more quantitative, dimen-

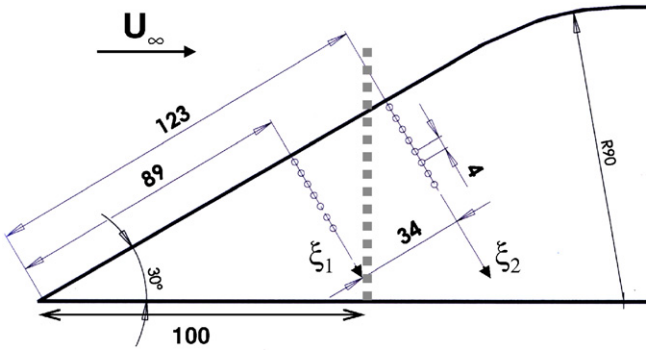

Fig. 2. Pressure holes machined in the lateral surface of the body (all dimensions in mm). The vertical dashed grey line corresponds to the location of the LDV measurement plane. ξ_1 and ξ_2 are the distances from the "A-pillar" sharp edge along lines 1 and 2.

Table 1
Location of the pressure tabs along lines 1 and 2

Line 1	$C_{1,1}$	$C_{1,2}$	$C_{1,3}$	$C_{1,4}$	$C_{1,5}$	$C_{1,6}$	$C_{1,7}$	–
ξ (mm)	2	6	10	14	18	22	26	–
Line 2	$C_{2,1}$	$C_{2,2}$	$C_{2,3}$	$C_{2,4}$	$C_{2,5}$	$C_{2,6}$	$C_{2,7}$	$C_{2,8}$
ξ (mm)	2	6	10	14	18	22	26	30

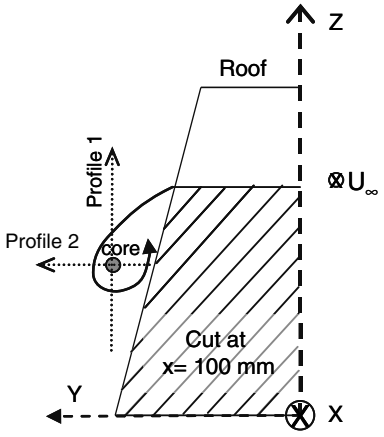

Fig. 3. Front view of the body in the LDV plane $x = 100$ mm.

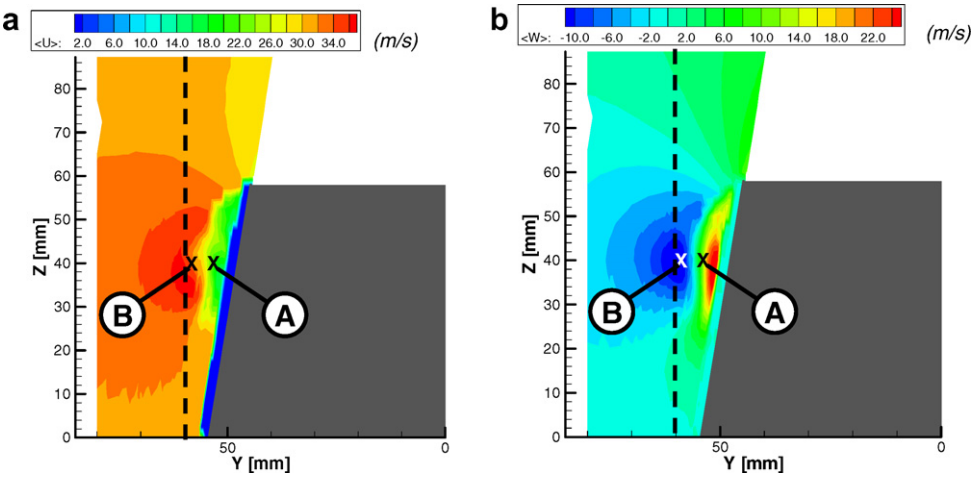

Fig. 4. Mean velocity field in the plane $x = 100$ mm. A and B are points selected for a detailed study – see Fig. 7 and 8. (a) $\langle U\rangle$ (m/s); (b) $\langle W\rangle$ (m/s).

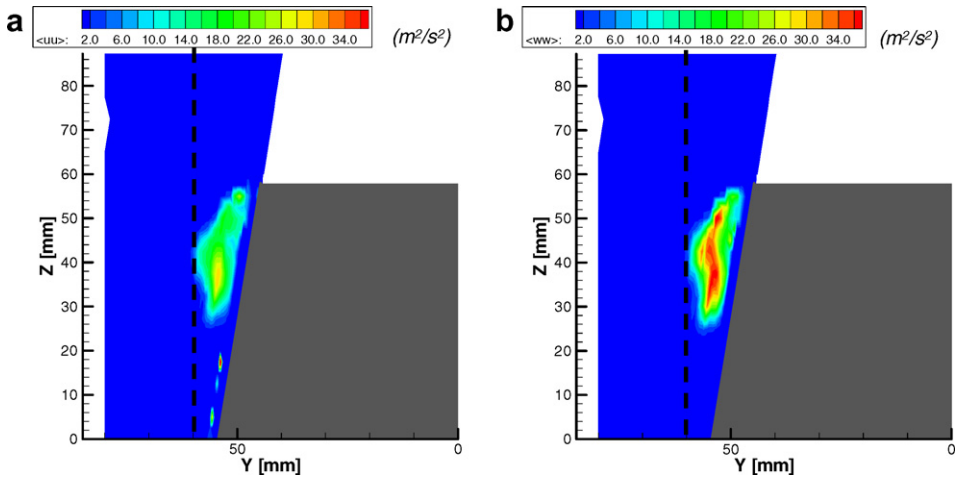

Fig. 5. Reynolds stresses in the plane $x = 100$ mm. (a) $\langle uu \rangle$ (m^2/s^2); (b) $\langle ww \rangle$ (m^2/s^2).

sionless quantities are plotted along horizontal and vertical profiles passing across the location of maximum longitudinal fluctuating velocity in Figs. 6 and 7. This maximum is located at $y \approx 54$ mm and $z \approx 40$ mm. Two maxima of $\langle uu \rangle / U_\infty^2$ and $\langle ww \rangle / U_\infty^2$ are observed on the vertical profile (Fig. 6). The first one, located at $z \approx 48$ mm, corresponds to the 3D shear layer separating from the sharp "A-pillar". The anisotropy is high with $\langle ww \rangle / \langle uu \rangle \approx 1.8$. This anisotropy is believed to be associated with a vertical flapping of the shear layer. The second peak is located in the core of the vortex. Vertical fluctuations in this region are again more intense than horizontal ones ($\langle ww \rangle / \langle uu \rangle \approx 1.5$). We also notice in Fig. 6 that u and w are negatively correlated (The correlation coefficient $R_{uw} = \langle uw \rangle / u'w'$ is $R_{uw} \approx -0.2$ in the core and $R_{uw} \approx -0.3$ in the shear layer wrapping around the vortex core). Understanding the fluctuating character of the velocity field in such a 3D situation is a complex problem. These fluctuations are indeed the result of (i) a high turbulence level generated in the 3D swept shear layer after flow separation at the sharp edges; (ii) an unsteady behaviour of the conical vortex itself interacting with the lateral wall of the body and (iii) a global coupling of the separated structures on the whole body. These contributions cannot be separated from

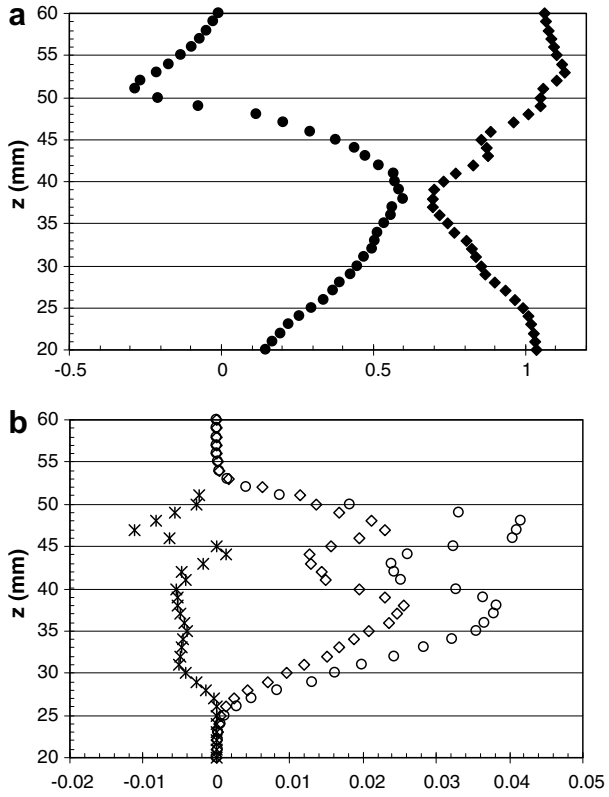

Fig. 6. Vertical profiles in the plane $x = 100$ mm. The lateral location is $y = 54$ mm. (a) Dimensionless mean velocity ♦ $\langle U \rangle / U_\infty$; ●, $\langle W \rangle / U_\infty$. (b) Dimensionless Reynolds stresses ◇, $\langle uu \rangle / U_\infty^2$; ○, $\langle ww \rangle / U_\infty^2$; *, $\langle uw \rangle / U_\infty^2$.

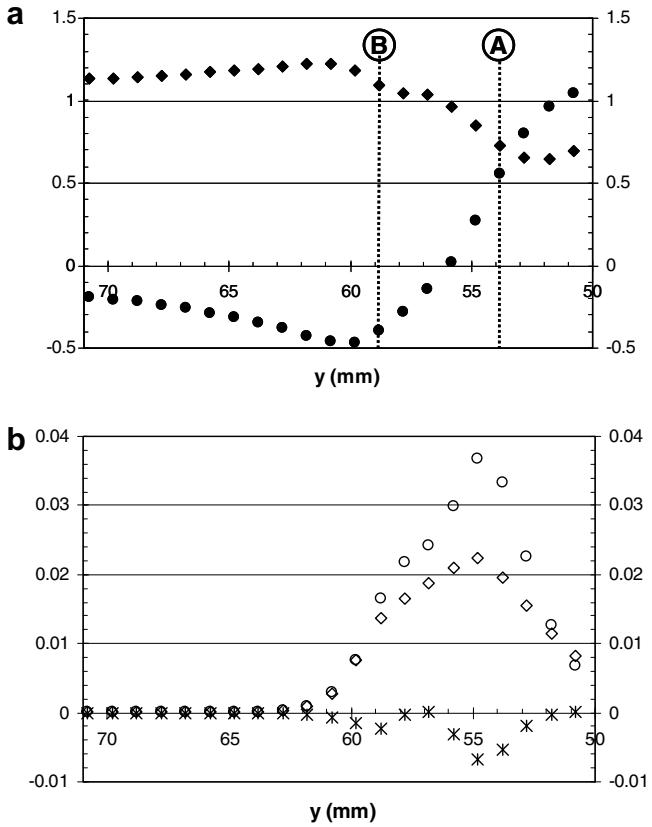

Fig. 7. Horizontal profiles in the plane $x = 100$ mm. The vertical location is $z = 40$ mm. (a) Dimensionless mean velocity ♦ $\langle U \rangle / U_\infty$; ●, $\langle W \rangle / U_\infty$. (b) Dimensionless Reynolds stresses ◇, $\langle uu \rangle / U_\infty^2$; ○, $\langle ww \rangle / U_\infty^2$; *, $\langle uw \rangle / U_\infty^2$.

single point velocity measurements. We will show in the following that the study of their spatio-temporal signature on the unsteady wall pressure field leads to interesting conclusions.

To give a more detailed description, two points shown in Figs. 4 and 7a have been selected on both sides of the mean centre of the vortex. The associated pdf of U and W and a cloud of (U, W) points are presented in Fig. 8. The left hand side of Fig. 8 corresponds to point A located in a region of strong positive $\langle W \rangle$. Nevertheless, the probability of finding negative values of W is non-zero and the pdf of W at that point is negatively skewed. On the contrary, point B is located at the edge of the structure (negative value of $\langle W \rangle$) but the probability of finding positive W is considerable while the pdf of W here is positively skewed. The signature of these extreme events is assumed here to be associated with a lateral and vertical meandering of the vortical structure, which engulfs vorticity from the 3D shear layer. At point A, the $\langle uw \rangle$ correlation is negative which means that high longitudinal velocities are associated (in a statistical sense) with negative vertical velocities. Noting that the interaction of the vortex core with the nearest side wall corresponds to a "mirror induced" velocity along the side wall and directed toward the sharp edge, such extreme events at point A could correspond to shrinkage of the separated structure along the sharp edge. On the contrary, no significant $\langle uw \rangle$ correlation is measured at the mean edge of the vortex (point B). The signature of this velocity field on the wall pressure is now considered.

4. Spatio-temporal properties of the fluctuating pressure field at the wall

Fluctuating pressure has been measured along the two transverse lines of Fig. 2. The fluctuating pressure coefficient $C_{p'} = \sqrt{\langle p^2 \rangle}/(\rho U_\infty^2/2)$ plotted in Fig. 9 was obtained by integrating the power spectral density (PSD) between 50 Hz and 5 kHz. Note indeed that fluctuating pressure measurements using off-set electret microphone cartridges are not accurate below 50 Hz. The abscissa in Fig. 9 is the distance ξ from the "A-pillar" sharp edge normalised by the mean reattachment distance ξ_R. The location of this mean reattachment was estimated from oil flow visualisation and can be approximated by a straight line originating from the front edge of the body and inclined at an angle of 20° with respect to the x axis. We see that our spatial discretization is not fine enough to smoothly resolve the evolution of C'_p. The two maxima are detected for $\xi/\xi_R < 1$ and, beyond these maxima, the evolution

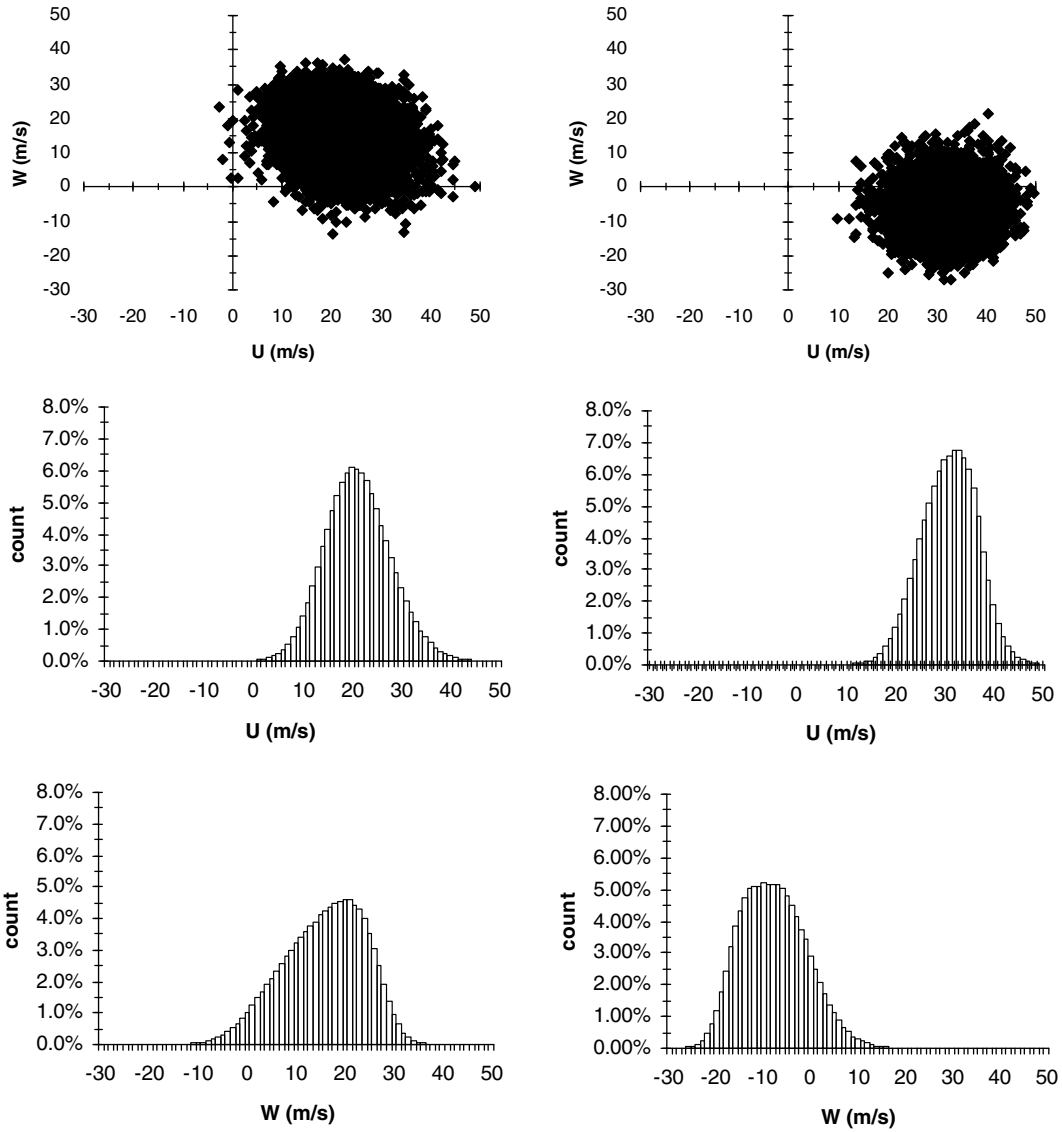

Fig. 8. pdf of U and W and cloud of (U,W) points at points A (left column) and B (right column) (see Figs. 4 and 7a).

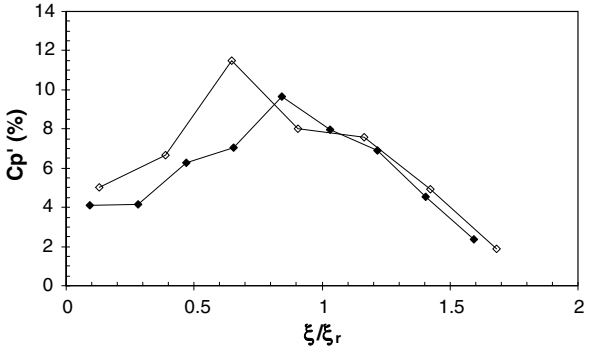

Fig. 9. Fluctuating pressure coefficient. The abscissa is the distance ξ from the "A-pillar" sharp edge normalised by the mean reattachment distance ξ_R. ◇, line 1; ♦, line 2.

of C_p' along the two lines is reasonably self-similar. The two maxima correspond respectively to the third pressure sensor of line 1 ($C_{1,3}$) and to the fifth sensor of line 2 ($C_{2,5}$). These two locations are considered next because it is important to study the development of the conical vortex along its axis and not "slice by slice".

Fig. 10a present both PSD at $C_{1,3}$ and $C_{2,5}$ and the modulus of the cross-spectrum. With the semi Log representation adopted here, we have, in a frequency domain $[f_1, f_2]$: $\int_{f_1}^{f_2} \mathrm{PSD}(f)\,\mathrm{d}f = \int_{f_1}^{f_2} f \cdot \mathrm{PSD}(f)\,\mathrm{d}Ln(f)$. This representation is therefore useful because the energy content is readily visualised. Fig. 10b shows the coherence between the two signals while Fig. 10c shows the phase evolution in the frequency domain (in the high frequency range, we restrict ourself to the domain where the coherence is larger than 0.1). At $C_{1,3}$, the PSD is maximum in the frequency band $f \in$ [1.5 kHz, 3 kHz]. The maximum shifts toward lower frequencies on the second transverse line and approximately spans the frequency interval $f \in$ [1.5 kHz, 2.5 kHz] at $C_{2,5}$. One interesting result is that the values of the cross-spectrum and of the coherence are very weak in these frequency bands. The physical phenomena responsible for these maxima are therefore only weakly correlated between the two sensors.

On the contrary, we observe a very clear local maximum of both PSD, of the cross-spectrum and of the coherence centred at $f \approx 1$ kHz. Moreover, even if the energy content is lower, the coherence between both signals is high in the low frequency region (very large peak centred at $f \approx 300$ Hz). In Fig. 10c, we measure a quasi-linear evolution of the phase angle with frequency. Indeed, the slight rupture is only measured in the region where the coherence is weak. This result will be discussed in the next section.

A synthetic view across the footprint of the structure on the wall is obtained by integrating the PSD and the interaction energy in the three distinct frequency bands [100 Hz, 700 Hz], [700 Hz, 1.5 kHz] and [1.5 kHz, 4 kHz]. Fig. 11a presents, from sensor $C_{1,1}$ to sensor $C_{1,5}$ along line 1, the fluctuating pressure energy $\int_{f_1}^{f_2} \mathrm{PSD}_{1,j}(f)\,\mathrm{d}f = \int_{f_1}^{f_2} \hat{p}_{1,j}(f)\hat{p}_{1,j}^*(f)\,\mathrm{d}f$ integrated in these $[f_1, f_2]$ frequency bands (full symbols) and the modulus of the integrated interaction energy $|\int_{f_1}^{f_2} \hat{p}_{1,j}(f)\hat{p}_{1,3}^*(f)\,\mathrm{d}f|$ of sensor $C_{1,j}$ with $C_{1,3}$ (empty symbols and dashed lines). $\hat{p}_{1,j}(f)$ is the Fourier transform of the pressure signal at sensor $C_{1,j}$ and $\hat{p}_{1,j}^*(f)$ its complex conjugate. In Fig. 11b, each interaction energy has been normalised by the local total interaction energy in the frequency band [100 Hz, 4 kHz] in order to emphasise the relative contribution of each frequency band. We see clearly that the "high frequency" contribution is dominant only in the neighbourhood of the reference sensor. On the contrary, the local relative contributions in the intermediate frequency band is approximately constant across the vortex structure while the relative contribution of the lower

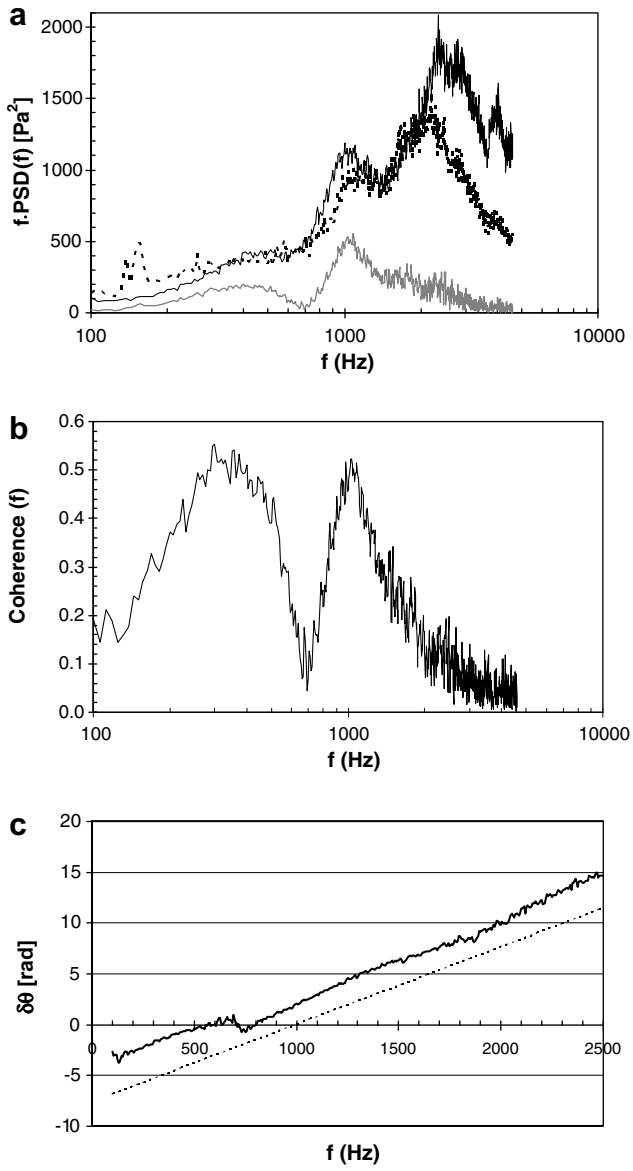

Fig. 10. (a) Power spectral densities at $C_{1,3}$ (–) and $C_{2,5}$ (- -) and modulus of the cross-spectrum (▬). (b) Coherence between the two signals. (c) Phase evolution in the frequency domain restricted to the domain where the coherence is larger than 0.1. The dashed straight line in (c) is introduced and discussed in part 5.

frequency part increases on the side of the conical structure. This shows that the corresponding physical events have a large scale transverse coherent signature.

The small size of the model used here however prevents us from obtaining a refined description along the transverse direction of the structure. Spatio-temporal properties of the pressure signal along the vortex core are therefore discussed in more depth in the next section.

5. Discussion

In 2D separated flows, the link between the velocity field and the fluctuating wall pressure field is clearly established (Kiya and Sasaki, 1983; Cherry et al., 1984; Hudy et al., 2003). In particular, large scale structures shed from the separated region are transported downstream and dissipate over the recovering boundary layer (Castro and Epik, 1998; Song et al., 2000) and their wall pressure signature is very clear (Hoarau et al., 2006). These results are

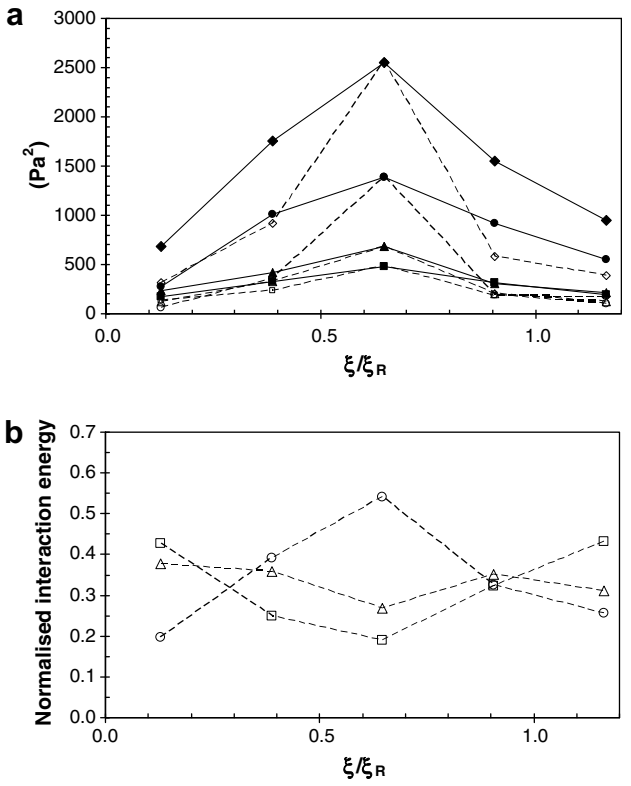

Fig. 11. Energy (filled symbols) and interaction energy (empty symbols) in the three distinct frequency bands: ♦, ◇, [100 Hz, 4 kHz]; ■, □, [100 Hz, 700 Hz]; ▲, △ [700 Hz, 1.5 kHz]; ●, ○, [1.5 kHz, 4 kHz]. (a) Transverse evolution along line 1. (b) Transverse evolution of the interaction energy along line 1 normalised by the local total interaction energy.

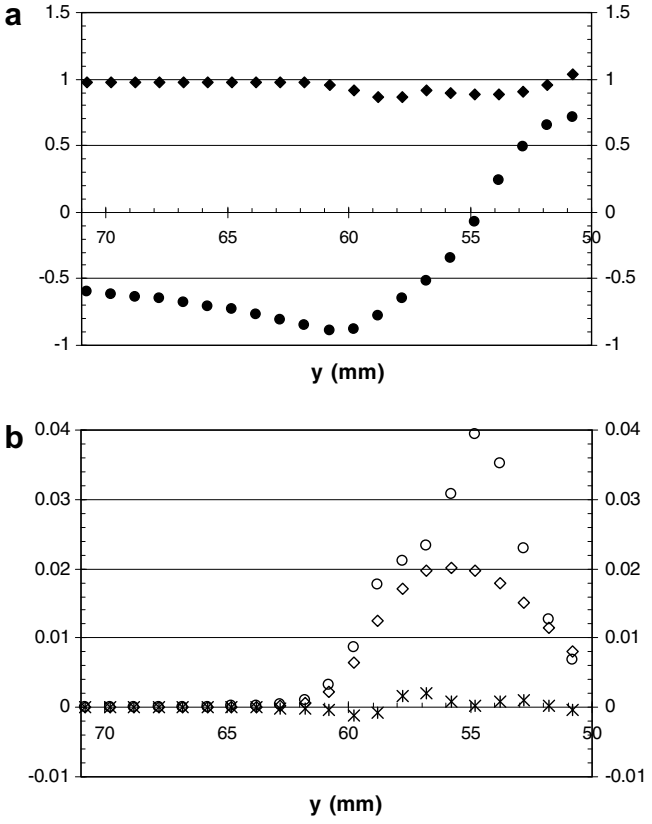

Fig. 12. Horizontal profiles of the components of the velocity field in a local referential aligned with the vortex axis. Profile in the plane $x = 100$ mm. The vertical location is $z = 40$ mm. (a) Dimensionless mean velocity ♦ $\langle U_a\rangle/U_\infty$; ●, $\langle W_a\rangle/U_\infty$. (b) Dimensionless Reynolds stresses ◇, $\langle u_a u_a\rangle/U_\infty^2$; ○, $\langle w_a w_a\rangle/U_\infty^2$; ⁎, $\langle u_a w_a\rangle/U_\infty^2$.

difficult to extend to fully 3D aerodynamic situations. However, we are here in a particular situation in which the wall pressure fluctuations are associated with perturbations of the conical vortex structure itself or to smaller scale perturbations transported by this particular flow structure. Let us conjecture here that the determination of the flow velocity field projected along the direction of the vortex core is important in this particular region of the flow field. We approximately locate the centre of the vortex at the point of maximum turbulence in the plane $x = 100$ mm: $(x, y) = (54$ mm, 40 mm). A straight line drawn from the corner of the nozzle of the body and passing through this point then has an angle of $\theta \approx 22°$ with the x-axis in a vertical plane and a small angle of $\varphi \approx 3°$ with the x-axis in a horizontal plane. Neglecting φ, we can obtain from the two-component LDV measurements the two components U_a and W_a of the velocity field, aligned, respectively with the vortex axis and perpendicular to it (in a vertical plane containing the axis). U_a and W_a read: $U_a = U\cos\theta + W\sin\theta$ and $W_a = -U\sin\theta + W\cos\theta$. Dimensionless mean and rms quantities are then computed and the horizontal profiles presented in Fig. 12a and b are associated with the data displayed in Fig. 7a and b. The mean rotation is clearly detected and we now see that the maximum of the rms values are located at $\langle W_a\rangle \approx 0$. Moreover, the magnitude of the vertically oriented rms velocities is significantly larger than the axially oriented rms velocities ($\langle w_a w_a\rangle/\langle u_a u_a\rangle \approx 2$) with a very small correlation coefficient $R_{u_a w_a} = \langle u_a w_a\rangle/u'_a w'_a$. Noticeably, the axial mean velocity $\langle U_a\rangle$ is quasi-constant across the core of the vortex with $\langle U_a\rangle \approx 28$ m/s. Considering again the wall pressure fluctuations discussed previously (Figs. 9a–c), we observe that, for perturbations transported by the velocity field at a constant mean velocity U_C, the phase difference $\delta\theta$ depends linearly on the frequency with: $\frac{\mathrm{d}\langle\delta\theta\rangle}{\mathrm{d}f} = 2\pi\frac{\Delta L}{U_C}$. Such elementary relations seem difficult to apply to a 3D velocity field. However, we are here in a particular situation with a quasi-uniform mean velocity component when the velocity is projected in the direction of the axis of the conical vortex (see Fig. 12). The slope of the straight line drawn in Fig. 10c has thus been computed by assuming that perturbations are transported along the core of the vortex at the velocity $U_C = \langle U_a\rangle \approx 28$ m/s and by using the distance $\Delta L = 34$ mm between the pressure sensors. A very good agreement is observed and shows that the perturbations are guided and transported along the axis of the conical vortex at the mean axial velocity.

Representative length scales can be associated with both coherence peaks observed in Fig. 10b. For the low frequencies, $f \cdot L_1/U_C \approx 1$ with $U_C \approx 28$ m/s and $f \approx 300$ Hz leads to $L_1 \approx 90$ mm. The associated length scale is thus of the order of the full length of the conical structure and we might associate this contribution to a meandering of the structure. At intermediate frequencies, $f \cdot L_2/U_C \approx 1$ with $U_C \approx 28$ m/s and $f \approx 1$ kHz leads to $L_2 \approx 28$ mm. L_2 is of the order of the width of the structure (see Fig. 4) and might be associated with perturbations generated during the rolling-up of the unsteady vortex sheet (a 3D equivalent to vortex shedding) and transported along the core of the vortex. Note that the conical vortex is here a guide for these large scale perturbations in a 3D situation. Finally, let us consider the energy containing higher frequency part of the PSD. Signals associated with sensors $C_{1,3}$ and $C_{2,5}$ are only weakly correlated in this frequency band. We therefore conjecture that this contribution is due to a 3D turbulent field generated in the shear layers and uncorrelated between $C_{1,3}$ and $C_{2,5}$ because the turn over time scale is too short. One more hint supporting this hypothesis comes from the shift toward lower frequencies detected when comparing both PSD (Fig. 10a). If we

suppose that these physical events are associated with a similar Strouhal number scaling on the local reattachment length ξ_R, we should get $f_1\xi_{R1}/U_\infty \approx f_2\xi_{R2}/U_\infty \Rightarrow f_2/f_1 \approx \xi_{R1}/\xi_{R2}$. With $f_2 \approx 2$ kHz and $f_1 \approx 2.5$ kHz, one gets $f_2/f_1 \approx 0.8$ while $\xi_{R1}/\xi_{R2} \approx [89tg(20)/123tg(20)] \approx 0.72$ (see Fig. 2). The frequency shift is therefore expected to be due to the contribution of a turbulent field resulting from the development of the 3D shear layer and adapting itself to the development of the conical vortex.

6. Conclusion

The spatio-temporal properties of the unsteady wall pressure field of a model A-pillar conical vortex has been studied in this paper by combining 2 component LDV measurements and multipoint pressure measurements using off-set microphones. The model body has sharp edges. Detailed LDV measurements have been displayed in the vortex region. A conical vortex develops along the side walls of the body. Both the 3D shear layer separating from the sharp edges and the vortex core are highly unsteady regions. Moreover, the magnitude of the vertical rms velocities is significantly larger than the axial rms velocities. These fluctuating velocities are the signature of both an unsteady behaviour of the organised vortical structure interacting with the wall and of finer scale turbulence carried by the unsteady flow. We show that the spectral analysis – PSD, cross spectrum, coherence – of the fluctuating pressure at distant pressure sensors located near the line of maximal Cp' – that is to say under the vortex core – is useful for analysis of the link between the temporal and spatial scales of the unsteady aerodynamic and wall pressure field. In particular, we have shown that the conical vortex is a guide for the velocity perturbations and that their hydrodynamic pressure footprint is transported at the measured mean axial velocity in a local reference frame aligned with the vortex core. Two distinct peaks of coherence can then be associated with perturbations having (i) a length scale of the order of the full length of the conical structure; (ii) a length scale of the order of the transverse size of the structure. These perturbations may correspond to a global meandering of the structure (low frequency contribution) and to large scale perturbations generated during the rolling-up of the unsteady vortex sheet. Notably, the energy containing higher frequency parts of the PSD are only weakly correlated when distant sensors are considered. We notice that the associated physical events correspond to a similar Strouhal number, scaled on the local reattachment length. We therefore conjecture that they correspond to the contribution of a turbulent field resulting from the development of the 3D shear layer, adapting itself to the development of the conical vortex and uncorrelated between distant sensors because its length scale and turn over time scale is too short.

The three distinct contributions extracted here from the combined study of the pressure and velocity fields have a significant impact as far as Cp' is concerned and might be transmitted in very different ways by the car structure because the frequency and length scale range is very distinct. Energy transfer and non-linear interactions between these components are of course expected and were not studied here. We believe that this is a necessary step for a good understanding and eventually for the control of this unsteady aerodynamic.

Acknowledgements

The experiment was designed within the framework of a National Research group CNRT *"Recherche en Aérodynamique et Aéroacoustique pour les véhicules terrestres"* supported by Renault SA and PSA Peugeot-Citroen. C. Hoarau thanks the CNRT for financial support.

The technical support of P. Braud, F. Paillé and L. Philippon are warmly acknowledged. We thank the staff of the LEA Mechanical Workshop. Thanks to Peter Jordan for correcting the English.

References

Alam, F., Watkins, S., Zimmer, G., 2003. Mean and time-varying flow measurements on the surface of a family of idealised road vehicles. Exp. Therm. Fluid Sci. 27, 639–654.

Banks, D., Meroney, R.N., Sarkar, P.P., Zhao, Z., Wu, F., 2000. Flow visualization of conical vortices on flat roofs with simultaneous pressure measurements. J. Wind Eng. Ind. Aerodyn. 84, 65–85.

Castro, I.P., Epik, E., 1998. Boundary layer development after a separated region. J. Fluid Mech. 374, 91–116.

Cherry, N.J., Hillier, R., Latour, M., 1984. Unsteady measurements in a separated and reattaching flow. J. Fluid Mech. 144, 13–46.

Delery, J., 1994. Aspects of vortex breakdown. Prog. Aerosp. Sci. 30 (1), 1–59.

Depardon, S., Lasserre, J.J., Brizzi, L.E., Borée, J., 2006. 1/4 scale vehicle wake pattern analysis using near-wall PIV. SAE Trans. J. Passenger Cars Mech. Syst.. 2006-01-1027.

Gillieron, P., 2000. Analyse, modélisation et typologie des écoulements de culot dans l'automobile. AAAF-36eme Colloque d'Aérodynamique Appliquée, 20–22. Mars.

Hoarau, C., 2006. Mesures multipoints pression-vitesse pour l'analyse de l'aérodynamique d'écoulements décollés instationnaires. Application aux véhicules terrestres. Ph. D. Thesis, University of Poitiers.

Hoarau, C., Borée, J., Laumonier, J., Gervais, Y., 2006. Analysis of the wall pressure trace downstream of a separated region using extended proper orthogonal decomposition. Phys. Fluids 18, 5.

Hucho, W.H., 1998. Aerodynamics of Road Vehicles. SAE Int..

Hudy, L.M., Naguib, A.N., Humphreys, W.M., 2003. Wall-pressure-array measurements beneath a separating/reattaching flow region. Phys. Fluids 15–3, 706–717.

Kawai, H., Nishimura, G., 1996. Characteristics of fluctuating suction and conical vortices on a flat roof in oblique flow. J. Wind Eng. Ind. Aerodyn. 71, 579–588.

Kiya, M., Sasaki, K., 1983. Structure of a turbulent separation bubble. J. Fluid Mech. 137, 83–113.

Laumonier, J., Goudeau, C., Gervais, Y., 2001. Mesures aérodynamiques sur profil NACA 0012 avec décollement. 2001. In: Colloque Bruit des Ventilateurs à Basse Vitesse, Ecole Centrale de Lyon, November.

Lehugeur, B., Gillieron, P., 2006. Drag reduction by active control of A-pillar vortex breakdown on a simplified car geometry. In: European Drag Reduction and Flow Control Meeting. 10–14 April, Ischia, Italy.

Ol, M.V., Gharib, M., 2003. Leading-edge vortex structure of nonslender delta wings at low Reynolds number. AIAA J. 41 (1), 16–26.

SAEJ2071, 1994. Surface vehicle information report SAE, aerodynamic testing of road vehicles – Open throat wind tunnel adjustment.

Song, S., DeGraff, D.B., Eaton, J.K., 2000. Experimental study of a separating, reattaching, and redeveloping flow over a smoothly contoured ramp. Int. J. Heat Fluid Flow 21, 512–519.

Yavuz, M.M., Elkoury, M., Rockwell, D., 2004. Near-surface topology and flow structure on a delta wing. AIAA J. 42 (2), 332–340.